Chemical Engineering Journal 525 (2025) 170175

Contents lists available at ScienceDirect

Chemical Engineering Journal

journal homepage: www.elsevier.com/locate/cej

Modified magnesium phosphate cement composed of hyaluronic acid and ultrasound-responsive nanocapsules with improved physicochemical and osteogenic properties

Junyan Yao [a,b,1], Bin Wang [c,1], Yanbin Zhao [a,b,e], Yingxi Xu [a,b], Cheng Wang [a,b], Jing Bai [a,b,d], Feng Xue [a,b], Paul K. Chu [e], Chenglin Chu [a,b,*]

[a] School of Materials Science and Engineering, Southeast University, Nanjing, 211189, China
[b] Jiangsu Key Laboratory for Advanced Metallic Materials, Southeast University, Nanjing, 211189, China
[c] Department of Orthopedics, Rudong People's Hospital, Nantong, 226400, China
[d] Institute of Medical Devices (Suzhou), Southeast University, Suzhou, 215163, China
[e] Department of Physics, Department of Materials Science and Engineering, and Department of Biomedical Engineering, City University of Hong Kong, Tat Chee Avenue, Kowloon, Hong Kong, China

ARTICLE INFO

Keywords:
Magnesium phosphate cement
Hyaluronic acid
Controlled release
Ultrasound response
Osteogenesis

ABSTRACT

Although magnesium phosphate cement (MPC) has good biocompatibility and degradability, its poor compressive strength and insufficient osteogenic capacity hamper clinical applications. In this study, ultrasound-responsive drug-loading nanocapsules composed of melatonin-containing mesoporous silica and a layer of Pluronic F127 and hyaluronic acid (HA) are incorporated into the cement to enhance the mechanical and biological properties. The melatonin release rate, which can be controlled by the ultrasound intensity and time, reaches 72.45 ± 1.57 % after 7 days at 2 W/cm^2. The simulated drug release may be based on reversible cleavage and polymerization of F127 under the cavitation effect of ultrasound. The modified cement exhibits a lower reaction temperature (31.41 ± 0.79 °C), longer solidification time (11.9 ± 0.78 min), higher compressive strength (30.19 ± 0.78 MPa), better injectability (90.36 ± 4.01 %), and improved degradation characteristics than the pure MPC due to the complexation effect and adsorption action of HA during hydration. *In vitro* experiments confirm the excellent antibacterial properties, cytocompatibility, as well as osteogenic capacity. The results reveal an effective strategy to develop multifunctional cement for orthopedic applications.

1. Introduction

As the population ages, the increasing incidence of orthopedic diseases such as osteoporosis and fractures has led to a significant demand for bone implants in clinical care [1,2]. Autologous and allogeneic bone grafts are widely used in bone defect treatment due to their outstanding osteogenic capacity, but they suffer from limited sources, immune rejection, and infection [3]. Therefore, there is an urgent need to develop more suitable artificial materials as alternatives.

Magnesium phosphate bone cement (MPC) is a type of inorganic bioceramics that has attracted attention due to its great mechanical strength, excellent adhesive properties, and suitable degradation rate [4,5]. The cement hardens through the hydration reaction between magnesium oxide (MgO) and phosphates [6]. In order to reduce the reaction temperature and the toxicity of the products, MgO is usually calcined, and potassium dihydrogen phosphate (KH_2PO_4) is chosen for the reaction of $MgO + KH_2PO_4 + 5H_2O \rightarrow MgKPO_4{\cdot}6H_2O$ [7]. However, owing to the strong concentration gradients in the proximity of the MgO grains, the hydration reaction occurs far from equilibrium, resulting in a high reaction rate and the release of significant heat [8]. The short curing time, vigorous reaction, and limited osteo-inductivity of MPC restrict wider applications. It is therefore necessary to use materials with retardation function to control the rate, thereby modulating the heat release and extend operating time. To meet clinical demands, biocompatible substances like carboxymethyl chitosan-sodium alginate (CMCS/SA) gel [9], amino acids [10] and silk fibroin (SF) nanofibers

* Corresponding author at: School of Materials Science and Engineering, Southeast University, Nanjing, 211189, China.
E-mail address: clchu@seu.edu.cn (C. Chu).
[1] These authors contributed equally to this work

https://doi.org/10.1016/j.cej.2025.170175
Received 19 August 2025; Received in revised form 25 October 2025; Accepted 25 October 2025
Available online 27 October 2025

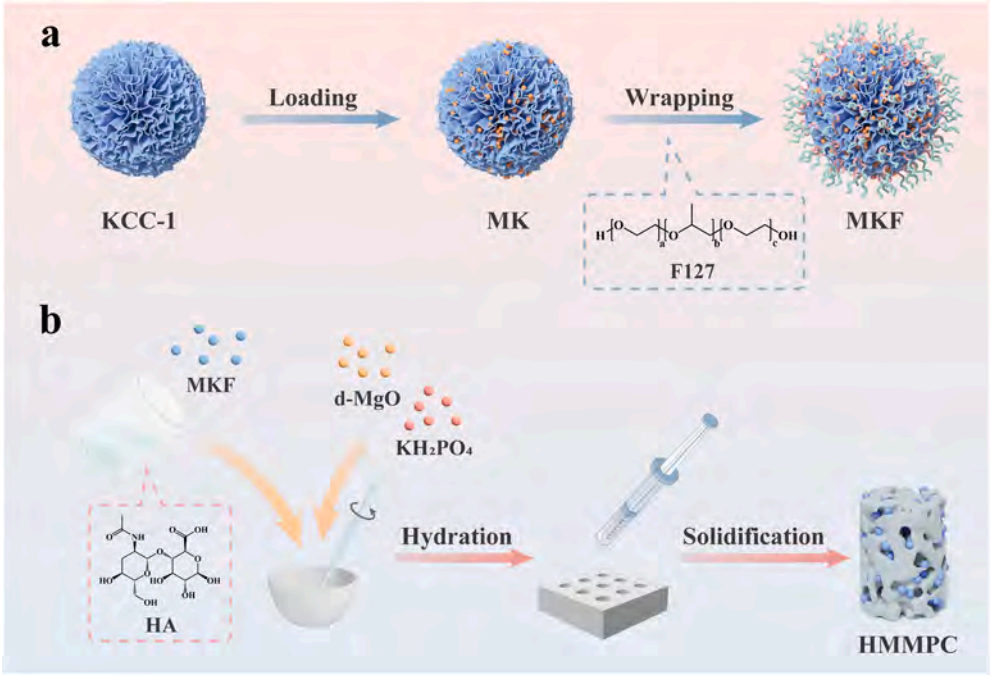

Fig. 1. (a) Synthesis of the drug-loaded ultrasound-responsive nanocapsules. (b) Preparation of modified MPC.

[11] have been incorporated into MPC to improve the physicochemical properties. Additionally, it is reported that drug-loaded microspheres [12] or hydrogels [13] have been introduced into MPC to establish a sustained drug release system to encourage osteogenesis. Nevertheless, the modification mechanisms of these complexes are rarely discussed, and the currently employed sustained release is insufficiently effective. Therefore, it is valuable to further investigate the role of integrated materials and advances in drug release methods.

Hyaluronic acid (HA) is an acidic glycosaminoglycan composed of D-glucuronic acid and *N*-acetylglucosamine that exists in the human body [14,15]. The HA solution is highly viscoelastic and has negatively charged carboxyl and hydroxyl groups, which, according to studies on similar macromolecules, may adsorb the cement particles and form complexes with Mg^{2+} [16,17]. These two effects produce excellent retardation properties. Meanwhile, as a biocompatible polymer, HA is widely used in tissue engineering, drug delivery, and orthopedic therapy [18–20]. It has been reported to interact with the cellular surface marker CD44 to promote cell proliferation and differentiation [21]. Therefore, the introduction of HA into MPC enhances the physicochemical and osteogenic capacities of bone cement.

Although HA improves the operability of MPC, it still fails to address the issue of limited osteogenic capacities. Therefore, this study further incorporates ultrasonic-responsive nanoparticles to achieve synergistic enhancement. Melatonin is a hormone which inhibits bone loss and promotes new bone formation by activating the melatonin receptor 2 [22]. In order to maintain the stability and activity of melatonin, it can be loaded into fibrous nanosilica spheres (KCC-1) [23]. However, the release rate of directly doped drugs is high initially but decreases sharply subsequently, resulting in short-term effects. Therefore, a stimuli-induced drug delivery system has been proposed [24,25]. In this system, drugs are encapsulated in stimuli-responsive polymers. When the drug-carrying capsules are transported to the target site, the polymers will be physically altered or chemically disrupted under endogenous (pH, enzymes, and temperature) or exogenous (light, ultrasound, and magnetic fields) stimuli, consequently opening the encapsulation switch to release drugs [26–29]. Among the various stimuli, ultrasound has the advantage of being non-invasive, modifiable, and deep tissue penetration, boding well for drug delivery [30,31].

Herein, HA and drug-loaded nanoparticles are incorporated into MPC in order to improve the physicochemical properties and osteogenic capacity. The nanosilica spheres KCC-1 are loaded with melatonin and wrapped with the ultrasound-responsive polymer F127 ($HO(C_2H_4O)_a(-C_3H_6O)_b(C_2H_4O)_cH$), as shown in Fig. 1. The drug release behavior is investigated and the degradation, cytocompatibility, antibacterial capability, and osteogenic capacity of MPC and relevant mechanisms are determined.

2. Materials and methods

2.1. Materials

Light magnesium oxide (*l*-MgO, *Mw*: 40.3 g/mol, 98 %) and potassium dihydrogen phosphate (KH_2PO_4, *Mw*: 136.09 g/mol, ^{3} 99.0 %) were purchased from Sinopharm Chemical Reagent Co., Ltd. Hyaluronic acid (*Mw*: 403.31 g/mol, ^{3} 99.0 %) and tetraethyl orthosilicate (TEOS, *Fw*: 208.33 g/mol, 99 %) were brought from Shandong Xiya Chemical Technology Co., Ltd. and 1-pentanol (*Mw*: 88.15 g/mol, 99 %) was produced by Shanghai Samarium Chemical Technology Co., Ltd. Melatonin (*Mw*: 232.28 g/mol, 98 %) was provided by Shanghai Meryer Biochemical Technology Co., Ltd. and hexadecyl trimethyl ammonium bromide (CTAB, *Mw*: 364.45 g/mol, 99 %) was obtained from Shanghai Macklin Biochemical Co., Ltd. Cyclohexane (*Mw*: 84.16 g/mol, 99.5 %) and 2-[2-(2-hydroxyethoxy)propoxy]ethanol (Pluronic F127, *Mw*: 12000 g/mol, 99.5 %) were acquired from Shanghai Aladdin Biochemical Technology Co., Ltd. And urea (*Mw*: 60.04 g/mol, 99 %) was provided by Shanghai Yuanye Biotechnology Co., Ltd. All the reagents were used without further purification and deionized water was produced by a Milli-Q water system.

2.2. Synthesis of nanoparticles

KCC-1 was prepared by the surfactant-templated and hydrothermal method. TEOS (2.5 g) and 1-pentanol (1.5 mL) were added to cyclohexane (30 mL) to form solution A, and CTAB (1 g) and urea (0.6 g) were dissolved in deionized water (30 mL) to produce solution B. Solutions A and B were mixed and magnetic stirred at 500 rpm for 30 min at room

Table 1
RT-PCR primer sequences.

Genes	Forward (5′ – 3′)	Reverse (5′ – 3′)
Runx2	GACTGTGGTTACCGTCATGGC	ACTTGGTTTTTCATAACAGCGGA
ALP	TCCGTGGGCATTGTGACTAC	TGGTGGCATCTCGTTATCCG
OCN	GGTAGTGAACAGACTCCGGC	GGCGGTCTTCAAGCCATACT
Col1A1	TTCTGCTGCTAATGTTCTTGACC	GGGATGAAGTATTGTGTCTTGGG

temperature (RT). The mixture was transferred to a Teflon reactor and heated to 120 °C for 4 h. The precipitate collected by centrifugation was washed with deionized water and ethanol, dried, and calcined at a rate of 2 °C/min to 550 °C and held for 6 h to obtain KCC-1. KCC-1 was dispersed in a melatonin ethanol solution (5 mM) and magnetic stirred at 500 rpm for 5 h. The melatonin-loaded KCC-1 (MK) was obtained by centrifugation and drying, while the filtrate was measured for free melatonin. The MK was dispersed in the F127 aqueous solution (0.5 mM) and magnetic stirred at 500 rpm for 30 min to form the F127-encapsulated MK (MKF). The UV absorption peaks of melatonin were monitored on a dual-beam ultraviolet-visible spectrophotometer (UV–vis, TU-1901, China) to establish the relationship between the absorbance and concentration and calculate the drug mass. The loading capacity (LC) and encapsulation efficiency (EE) were calculated by eqs. (1) and (2).

$$LC\ (\%) = \frac{m_0 - m_1}{m_2} \times 100\% \quad (1)$$

$$EE\ (\%) = \frac{m_0 - m_1}{m_0} \times 100\% \quad (2)$$

where m_0, m_1, and m_2 are the mass of total melatonin, free melatonin, and nanocontainers, respectively.

2.3. Characterization of nanoparticles

The crystal structure of KCC-1 was determined by X-ray diffraction (XRD, Rigaku Smart Lab SE, Japan) using Cu-K_α radiation and 2θ of 10–80°. Field-emission scanning electron microscopy (FE-SEM, Nova Nano SEM 450, USA) and transmission electron microscopy (TEM, Talos F200X S/TEM, USA) were used to analyze the morphology and microstructure. The functional groups and valence states were determined by Fourier transform infrared spectroscopy (FTIR, Thermo Scientific Nicolet iS10, USA) and X-ray photoelectron spectroscopy (XPS, Thermo Scientific K-Alpha, USA). The N_2 adsorption-desorption test was conducted to measure the Brunauer-Emmett-Teller (BET) surface area, and the pore size distribution was calculated according to the Barrett-Joyner-Halenda (BJH) method. The particle size distribution was analyzed by dynamic light scattering (DLS, Malvern Zetasizer Nano ZS90, UK).

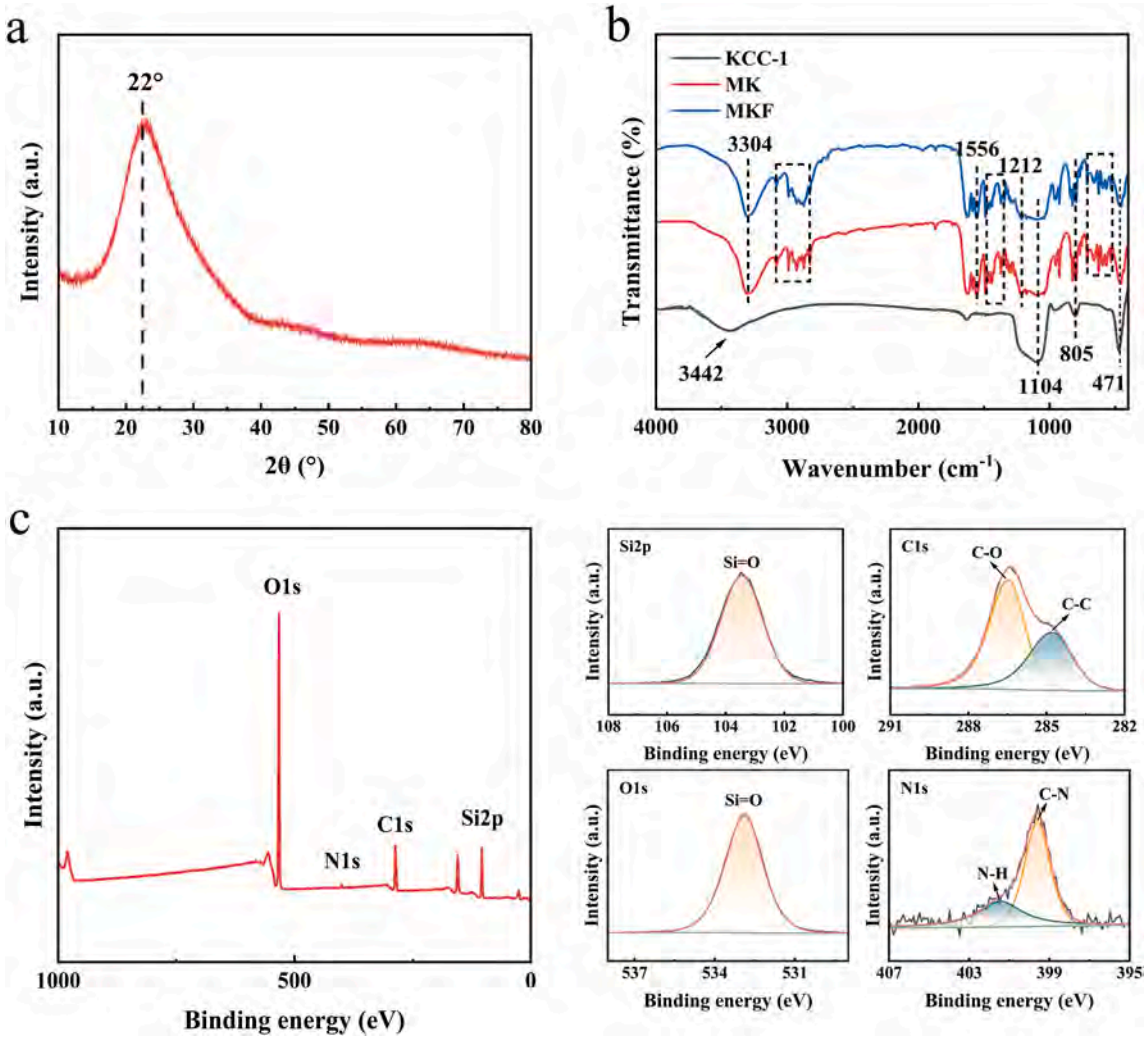

Fig. 2. Composition of nanoparticles: (a) XRD spectrum of KCC-1; (b) FTIR spectra of KCC-1, MK, and MKF; (c) XPS spectra of MKF.

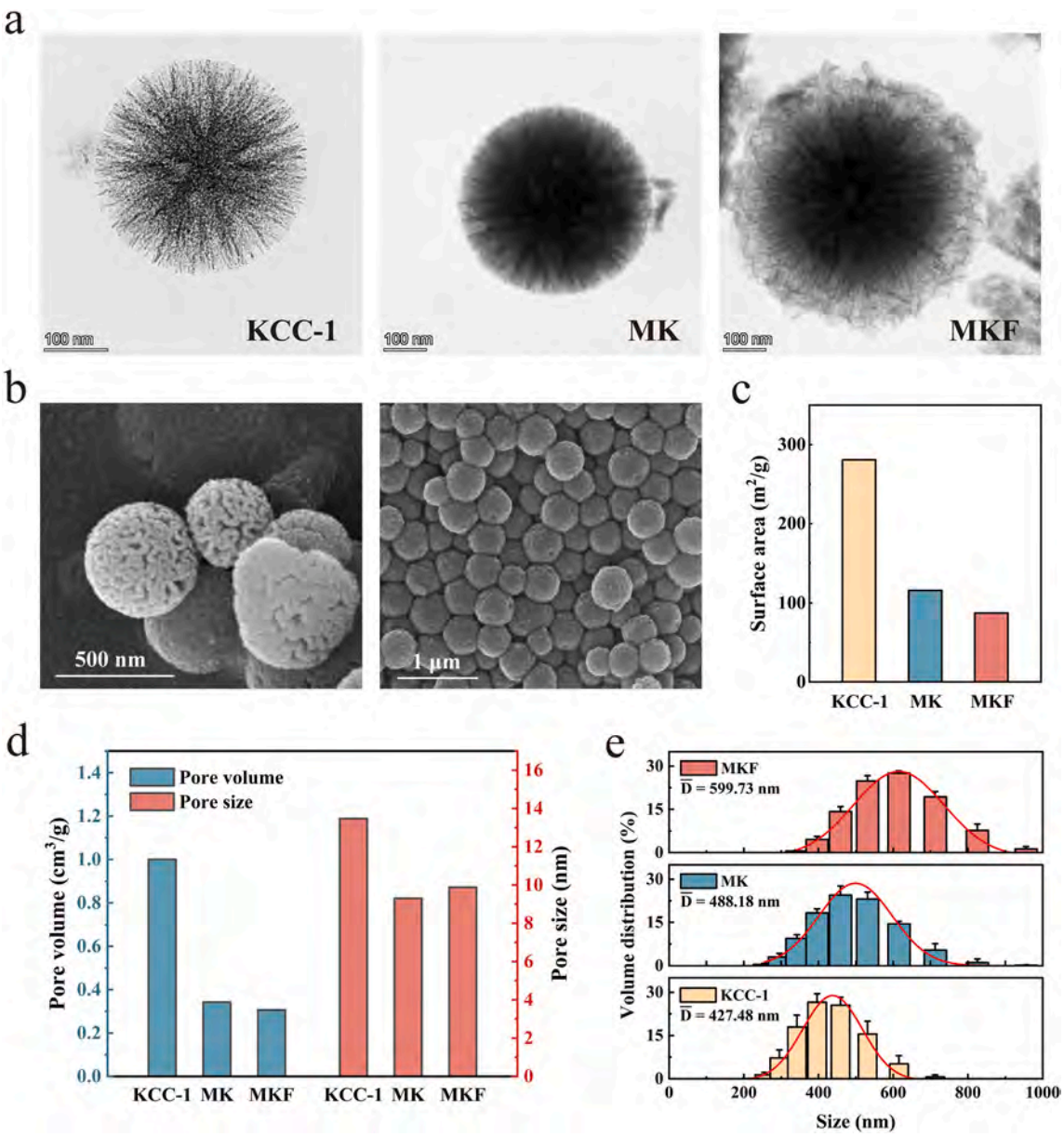

Fig. 3. Morphology and microstructure of nanoparticles: (a) TEM images of KCC-1, MK, and MKF. (b) SEM images of KCC-1. (c) Surface area, (d) Pore volume and pore size, and (e) Particle size distributions of KCC-1, MK, and MKF.

2.4. Ultrasound-induced drug release tests

The MK and MKF nanoparticles were placed in separate dialysis bags (MD-10, MW500D, USA) and submerged in the phosphate-buffered saline (PBS, pH = 7.4) at 37 °C for 7 days. The extracts were then exposed to ultrasound (1 Mhz) at different power densities (1.0, 1.5, and 2.0 W/cm^2) for 10 min on days 1, 3, 5, and 7. At the predetermined time points, the partial solution was taken out for measurement and an equal volume of fresh PBS was added. The cumulative release rate (CRR) at time point n was calculated by eq. (3).

$$CRR\ (\%) = \frac{C_n V + \sum_{i=1}^{n} C_i V_i}{m} \times 100\% \quad (3)$$

where C_n is the concentration of melatonin in solution at time point n, V and V_i are the volumes of PBS remaining and removed each time, and m is the mass of loaded melatonin.

Terephthalic acid (TA) dosimetry was performed to estimate the ultrasonic cavitation due to its fluorescent product of 2-hysroxyterephthalate ions (HTA). The TA solution was exposed to ultrasound (1Mhz) at different power densities (1.0, 1.5, and 2.0 W/cm^2) for 10 min and then determined by fluorescence photometry (F97pro, China). To verify the effect of heat generated by sonication, the MKF solution was heated to 37, 47, and 57 °C, and the drug release was monitored. The MW and distributions of F127 before and after sonication were determined by gel permeation chromatography (GPC, Agilent 1260, USA).

2.5. Preparation of cement

The solid phase of MPC consisted of dead-burned magnesium (*d*-MgO, produced by heating *l*-MgO to 1700 °C) and KH_2PO_4 with a mass ratio of 1.5: 1. They were sieved with an 80 mesh to acquire powder particles of ~180 μm after milling. The solid and liquid phases (deionized water, 10 mmol/L of HA solution, and 10 mmol/L of HA solution with 1 mg/mL of MKF) were mixed with a power/liquid ratio (PLR) of 20:3.8, stirred into a uniform phase, and transferred to cylindrical

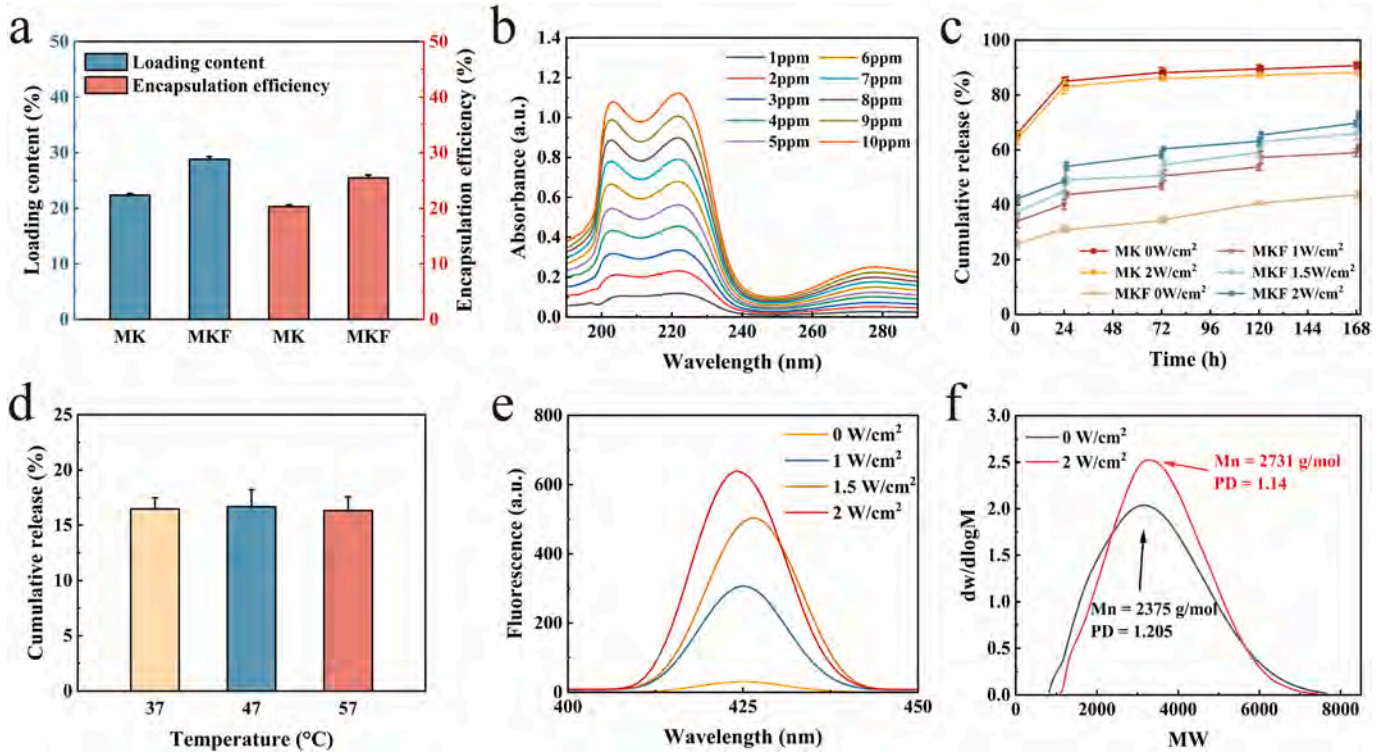

Fig. 4. Ultrasound-induced drug release and mechanism of MKF: (a) LC and EE of MK and MKF; (b) UV–vis plots of melatonin in the PBS solution; (c) Cumulative drug release from MK and MKF at different ultrasound intensities for 7 d; (d) Drug release from MKF at different temperatures for 10 min; (e) Ultrasound cavitation by TA dosimetry; (f) Mn and PD of F127 before and after sonication.

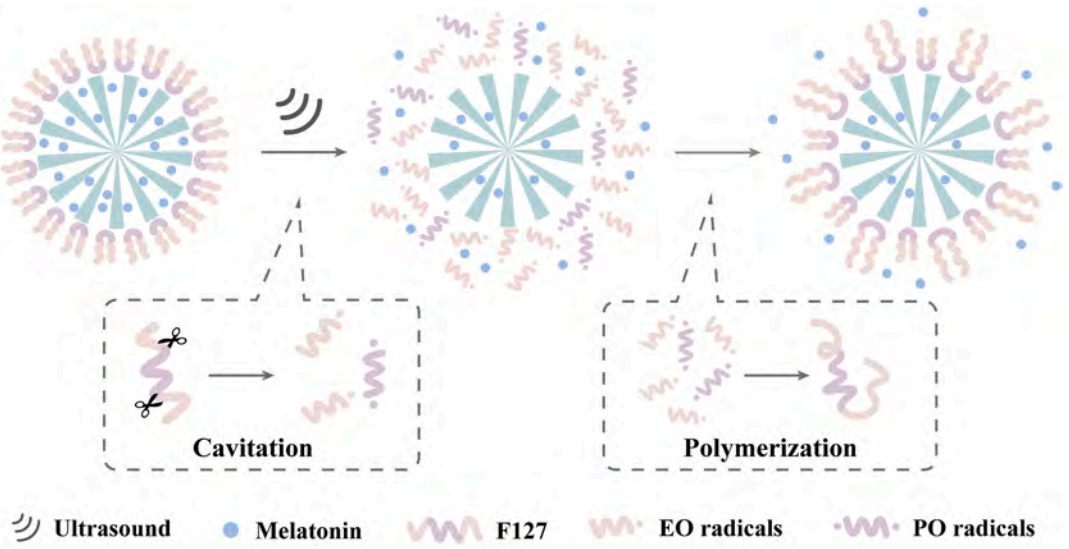

Fig. 5. Schematic diagram of the ultrasound-induced drug release mechanism.

silicone molds (f9 ´ 15 mm^3). After solidification, the specimens were cured at RT and 100 % relative humidity for 24 h. The cement samples were named MPC, HMPC, and HMMPC, respectively.

2.6. Characterization of cement

XRD was performed to determine the phase composition and FTIR was used to analyze the chemical composition. In addition, the surface morphology was examined by FE-SEM (FEI-Sirion, USA), and energy-dispersive X-ray spectrometry (EDS) was conducted to determine the elemental composition.

The setting time of cement was measured on a Vickers meter according to the National standard GB/T1346–2001. Timing started when the two phases were mixed and ended when the test needle sank into the cement paste by 0.5 mm. The hydration temperature was recorded by a high-precision temperature sensor (DS18B20). The compressive strength was determined on a universal testing machine (XQY-II, China) at a loading rate of 1 mm/min. The porosity was analyzed by an electronic densimeter (AR-300G) and calculated according to Archimedes' principle as shown below:

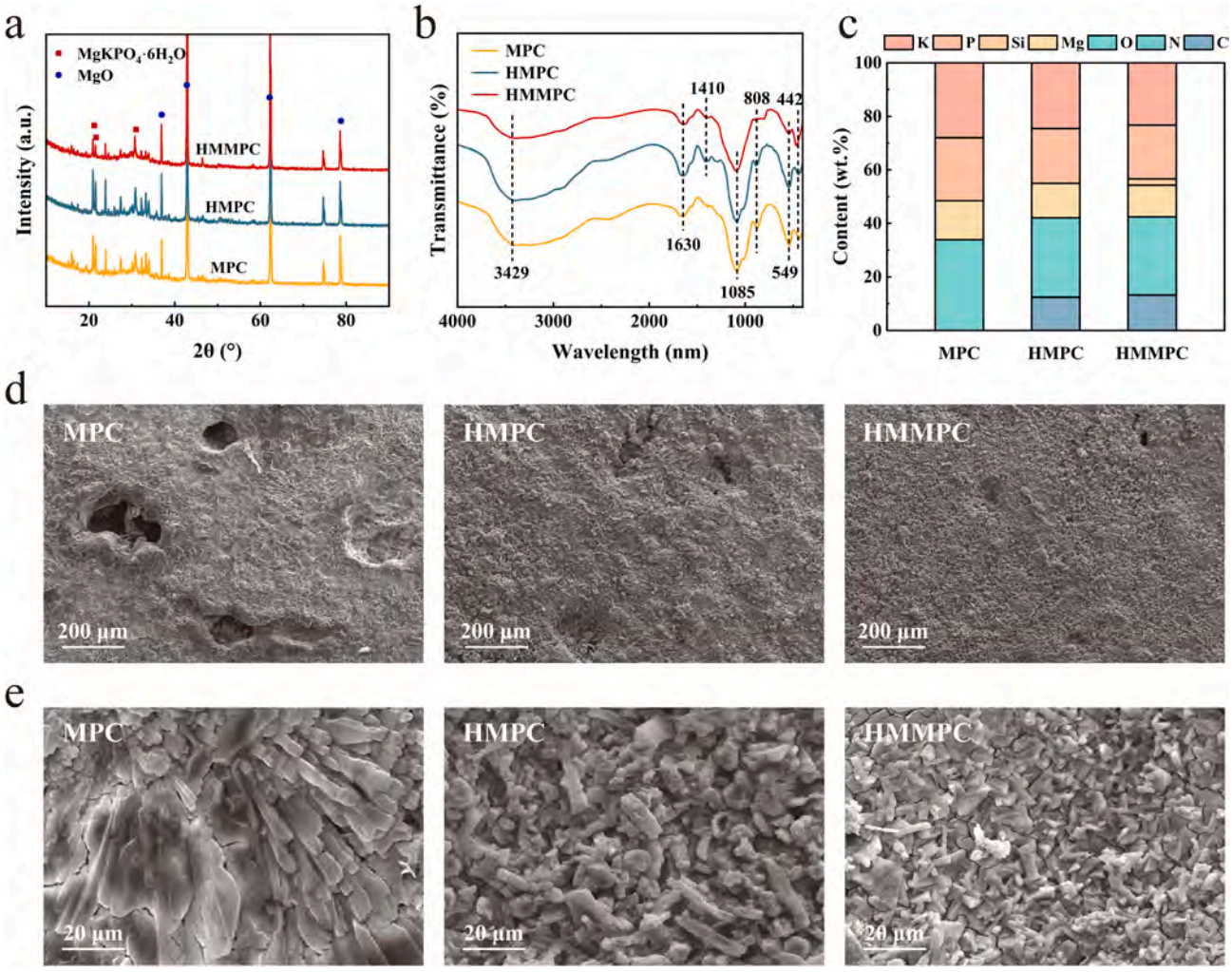

Fig. 6. Composition and morphology of cement: (a) XRD spectra; (b) FTIR spectra; (c) Element contents by EDS; SEM images of MPC, HMPC, and HMMPC at (d) 200× and (e) 2000×.

Table 2
EDS results of MPC, HMPC, and HMMPC.

Sample	C (wt%)	N (wt%)	O (wt%)	Mg (wt%)	Si (wt%)	P (wt%)	K (wt%)
MPC	–	–	33.91	14.54	–	23.56	27.99
HMPC	12.38	0.06	29.67	12.85	–	20.48	24.56
HMMPC	13.2	0.08	29.12	11.86	2.37	20.08	23.29

$$\text{Porosity}\ (\%) = \frac{w_2 - w_1}{w_2 - w_3} \times 100\% \quad (4)$$

where w_1 and w_2 are the mass of the cement before and after wetting, respectively, while w_3 refers to the mass of water being drained.

2.7. Conductivity and adsorption effects

The conductivity of the cement sample during the hydration reaction was measured by a conductivity meter (DDS-12DW, BANTE, USA). 10 g of the solid phase powder and 1.9 mL of liquid phase were added to 200 mL of deionized water, and the conductivity was recorded per minute. To investigate the complexation of Mg^{2+} by HA, the conductivity of $MgCl_2$ solution (5 mmol/L) with varying contents of HA was measured. The actual change in conductivity was obtained by subtracting the conductivity of HA itself from initial value. The adsorption effect was quantified using a total organic carbon (TOC) analyzer (multi N/C 3100, Analytik Jena, German). The slurry was pump-filtered when the hydration reaction started for 3 min and then the filtrate was assayed for the TOC content. The adsorption rate was calculated by eq. (5).

$$\textit{Adsorption rate}\ (\%) = \frac{c_0 - c}{c_0} \times 100\% \quad (5)$$

where c_0 and c are the TOC contents of the liquid phase and filtrate, respectively.

2.8. In vitro degradation

The cement specimens were immersed in the simulated body fluid (SBF) at 37 °C for 3 weeks with a solid-liquid ratio of 10: 1. The SBF was refreshed every other day in the first week and then weekly. The pH of the soaking solution was recorded before each change. The compressive strength, SEM images, and weight loss ratio (WLR) were assessed after vacuum drying.

2.9. Preparation of culture extract

A mixture of bone cement and complete cell/bacteria culture medium with a 0.2 g/mL ratio was extracted in an incubator (37 °C, 5 % CO_2) for 24 h. The extract was centrifuged at 4000 rpm for 10 min. The supernatant was collected after 0.22 μM membrane filtration.

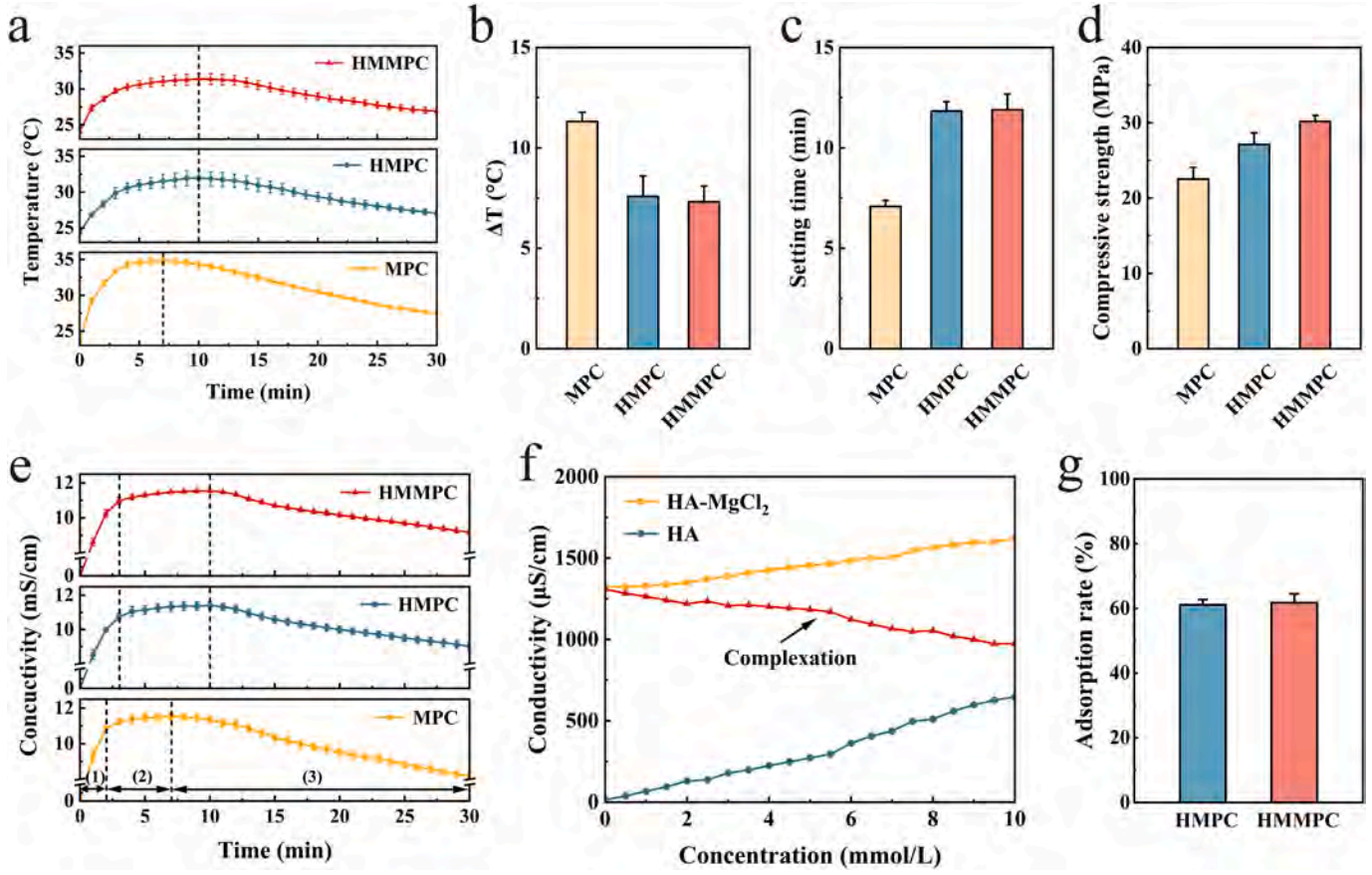

Fig. 7. Handling properties and hydration tests of MPC, HMPC, and HMMPC: (a) Temperature variation curves within 30 min during solidification; (b) Elevated temperature; (c) Setting time; (d) Compressive strength; (e) Conductivity within 30 min during the hydration reaction; (f) Influence of HA complexation on the conductivity of $MgCl_2$ solution; (g) Adsorption rates of HMPC and HMMPC.

Table 3
Injectivity and porosity of MPC, HMPC, and HMMPC.

Sample	Injection time (min)	Injection rate (%)	Porosity (%)	Density (g/cm^3)
MPC	5.36 ± 0.71	44.67 ± 5.96	26.81 ± 0.87	2.50 ± 0.04
HMPC	10.03 ± 0.98	83.58 ± 8.14	23.94 ± 0.84	2.60 ± 0.05
HMMPC	10.84 ± 0.48	90.36 ± 4.01	22.71 ± 0.52	2.74 ± 0.06

2.10. Bacteria killing assay

Gram-negative *E. coli* were used to measure the antibacterial effects by the spread plate-counting method. The bacterial suspensions were incubated at 37 °C overnight in a shaking incubator and diluted to 10^7 CFU mL^{-1} with the 0.9 % NaCl solution. After incubation for 15 h, the mixture was added to cuvettes and immersed for 4 h. 100 μL of the bacteria (10^5 CFU mL^{-1}) were spread on agar plates and incubated at 37 °C for 15 h. The bacteria-containing plates were photographed and the number of new bacteria colonies was counted.

2.11. Cell proliferation and viability

The CCK-8 and Calcein/PI methods were used to monitor the proliferation and viability of C3H10 cells. The CCK-8 cells were cultured on 96-well plates with a complete medium at a density of 1×10^3. The original medium was discarded after 1 day, and the extract was added. Afterward, on days 1, 3, and 5, 10 mL of the CCK-8 test liquid were added to each well, and after incubating in a cell incubator for 1 h, the absorbance was recorded on a microplate reader (450 nm). In the Calcein/PI method, the cells were cultured on 12-well plates until the density reached 80–90 %. The complete medium was removed and the plates were cleaned with PBS twice. Calcein/PI was added in a darkroom and observed by fluorescence microscopy.

2.12. Apoptosis

The C3H10 T1/2 cells were cultured in 6 wells with a density of 1×10^6. The original medium was discarded when the cell density reached 80 %. To determine the degree of apoptosis, the cells were washed twice with cold PBS and resuspended in 1 × binding buffer with a concentration of 1×10^6 cells/mL. They were transferred to 100 μL of the solution (1×10^5 cells) in a 5 mL culture tube. 5 μL of FITC Annexin V and 5 μL of PI were added. The cells were gently vortexed and incubated for 15 min at RT in the dark. 400 μL of the 1 × binding buffer were added to each tube, and flow cytometry was performed within 1 h.

2.13. ALP/ARS and quantitative analysis

The osteogenic induction fluid consisted of 500 μL of β-glycerophosphate (10 mM), 50 μL of dexamethasone (10 nM), and 100 μL pf ascorbic acid (50 μg/mL) in 50 mL of the extract. The original medium was discarded when the cell density reached 80 %, and then the induced medium was added and replaced every 2 days. The cells were cultured on a 6-well plate with a density of 2×10^6. The protein samples were prepared by the bicinchoninic acid (BCA) method. ARS staining was performed quantitatively on a microplate reader by monitoring the absorbance at 562 nm. The ALP activity was determined by culturing the cells on 96-well plates with a density of 1×10^3. The original medium

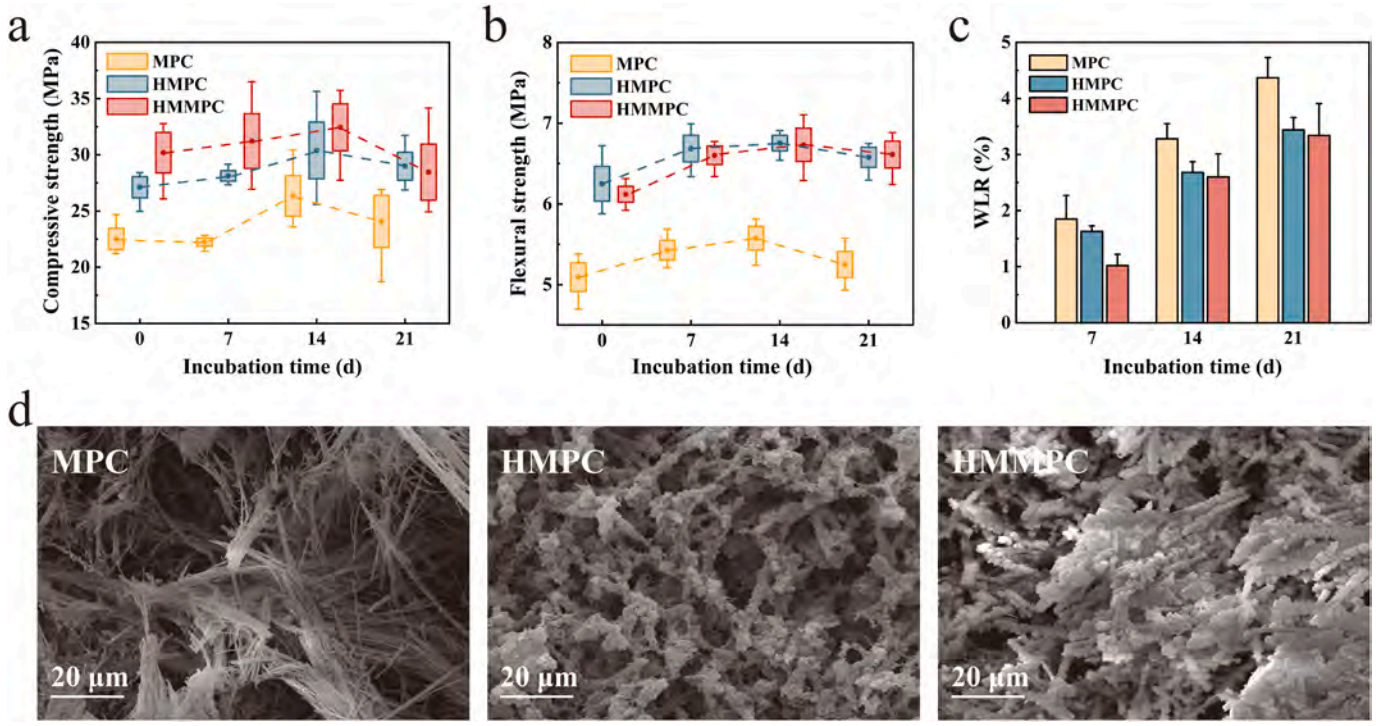

Fig. 8. *In vitro* degradation of MPC, HMPC, and HMMPC: (a) Compressive strength and (b) Flexural strength on days 0, 7, 14, and 21; (c) WLR on days 7, 14, and 21; (d) SEM images on day 21.

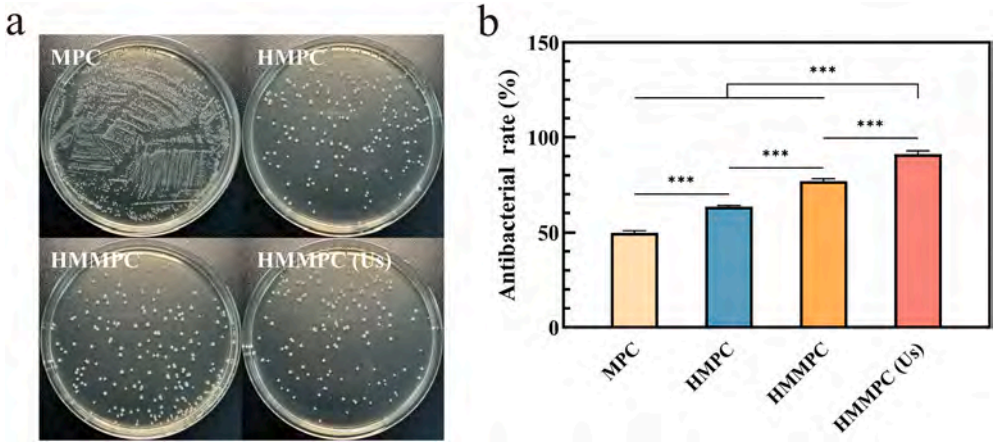

Fig. 9. (a) Photographs of gram-negative *E. coli* growth on MPC, HMPC, and HMMPC with and without 2 W/cm^2 ultrasound for 10 min; (b) Bactericidal rates calculated by colony plate counting (*$p < 0.05$, **$p < 0.01$, and ***$p < 0.001$).

was discarded before staining, and the cells were cleaned twice with PBS. The lysis solution was added, and the supernatant was collected by centrifugation. It was mixed with the detection regent and incubated for 30 min at RT (dark environment). The absorbance at 405 nm was measured on a microplate reader.

2.14. Real-time PCR

The total RNA was extracted from the cells by the Trizol method and reverse transcribed into cDNA. Using Gapdh as the internal reference, the qPCR experiments were conducted to detect the expression level of osteogenic differentiation characteristic genes in the C3H10 T1/2 cells. The primers are shown in Table 1.

2.15. Statistical analysis

The data were expressed as mean ± standard deviation, and the statistical differences between three or more groups were analyzed by one-way analysis of variance (ANOVA) and Bonferroni *post hoc*. The significance of the difference between two groups was determined by the *t*-test. Statistical analysis was conducted using the SPSS software 19.0, and the statistical significance was defined as *p < 0.05, **p < 0.01, ***$p < 0.001$.

3. Results and discussion

3.1. Nanoparticles characterization

The composition, morphology, and microstructure of the

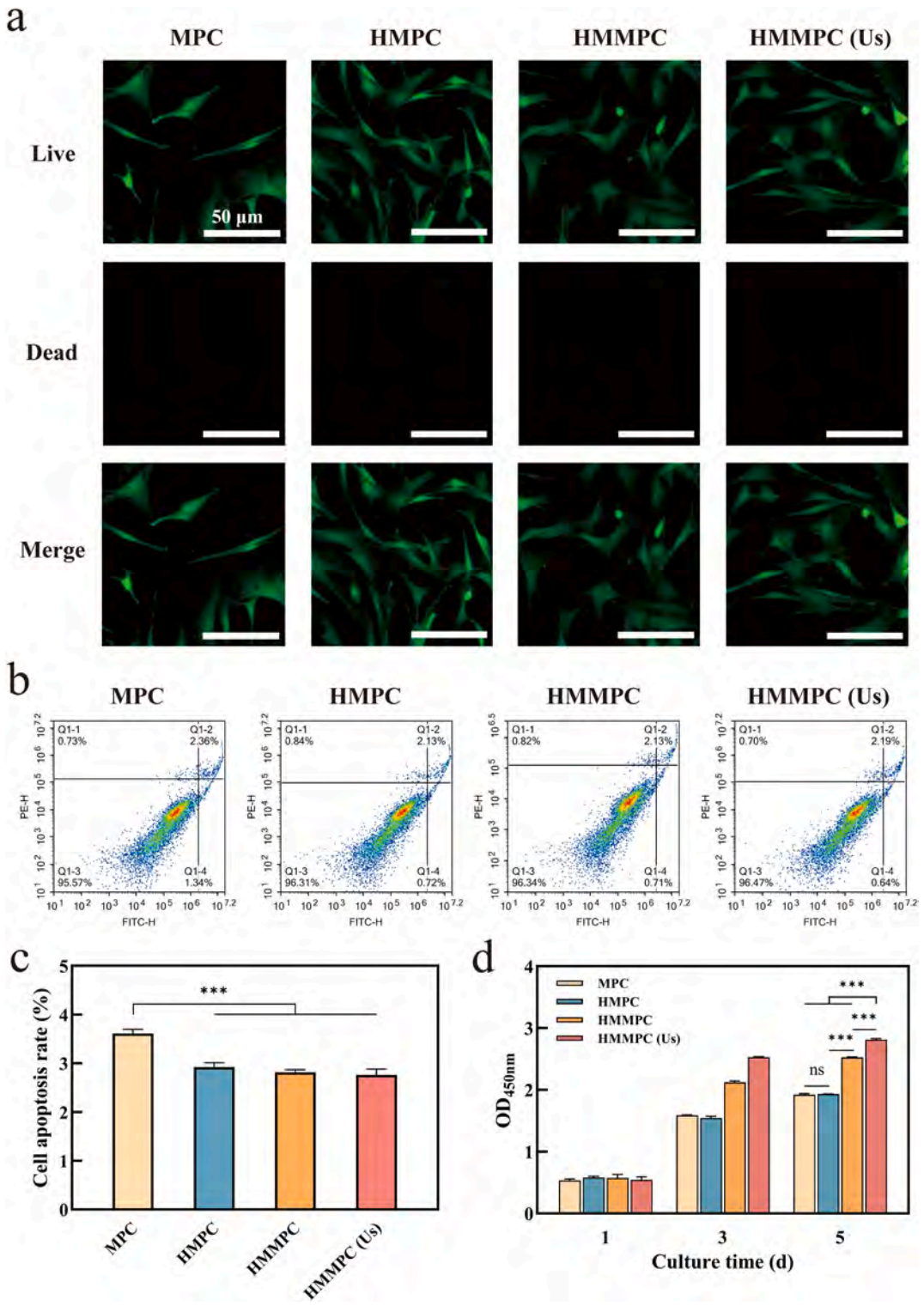

Fig. 10. *In vitro* biocompatibility of C3H10T1/2 cells treated with cement extracts: (a) Live/dead staining; (b) Cell apoptosis by flow cytometry; (c) Cell apoptosis rates; (d) CCK-8 analysis (*$p < 0.05$, **$p < 0.01$, and ***$p < 0.001$).

nanoparticles were analyzed. The XRD spectrum of KCC-1 in Fig. 2(a) shows only one broad peak around 22°, corresponding to the disordered structure of amorphous silica. As shown in Fig. 2(b), the FTIR spectra of the three nanoparticles reveal H-O-H (broad band between 3500 and 3200 cm^{-1}) as well as Si-O-Si asymmetrical (1104 cm^{-1}) and symmetrical (805 and 471 cm^{-1}) stretching vibrations from mesoporous silica. The peaks at 3100–2710 cm^{-1} and 1490–1245 cm^{-1} of MK and MKF indicate C—H groups. The 1556 cm^{-1} peak denotes C—N stretching, and the N—H bending peak of the amide coincides. The peak at 1212 cm^{-1} stems from C-O-C of the 1,2,4 tri-substituted benzene ring in melatonin. XPS is used to determine the chemical states of MKF (Fig. 2c). The survey spectrum shows O, Ni, C, and Si. The Si 2*p* and O 1 *s* spectra exhibit only Si—O (103.45 and 532.89 eV), suggesting physical adsorption to the drug and polymer. The C-O-C (286.35 eV) and C—C (284.76 eV) peaks in the C 1 *s* spectrum and N—H (401.45 eV) and C—N (399.61 eV) peaks in the N 1 *s* spectrum confirm the existence of melatonin and F127 in

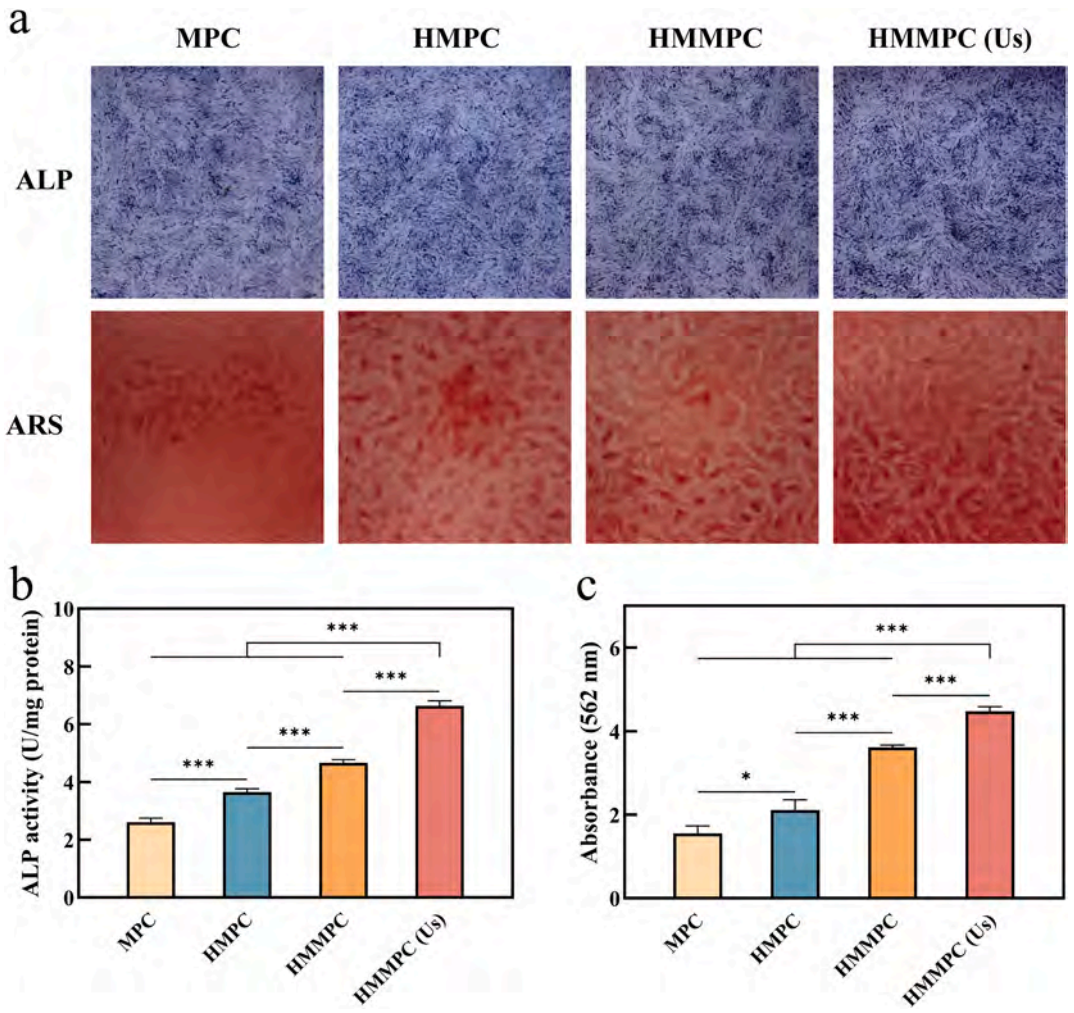

Fig. 11. Evaluation of the osteogenic properties of MPC, HMPC, HMMPC, and HMMPC (Us): (a) ALP and ARS staining; (b) Quantitative ALP activity; (c) Quantitative ECM mineralization by ARS (*$p < 0.05$, **$p < 0.01$, and ***$p < 0.001$).

MKF. The results confirm that KCC-1 nanoparticles are synthesized and the drug-loaded nanocapsules are prepared successfully.

The TEM images in Fig. 3(a) depict the microstructure of the nanoparticles. The spherical KCC-1 has a radial structure from the center with a large number of mesopores and channels. The holes in MK are filled with melatonin and the MKF was further entangled with a layer of F127. The SEM images of KCC-1 show that the sphere is formed by fibers in a 3D manner (Fig. 3b), giving rise to a porous morphology. According to the N_2 adsorption-desorption test, the BET surface area, pore volume, and pore size of KCC-1 are 280.74 m^2/g, 1.00 cm^3/g, and 13.47 nm, respectively (Fig. 3c, d), while those of MK and MKF decrease. Compared to the other mesoporous silica, KCC-1 has a larger space and sufficient sites supported by the fibrous structure for macromolecular drug loading and polymer wrapping [32]. The DLS results in Fig. 2(e) show that the mean diameters of the KCC-1, MK, and MKF particles are 441.83, 478.7, and 582.84 nm, indicating the successful packing of melatonin and the formation of an F127 film about 70 nm thick.

3.2. Ultrasound-induced drug release assay

The ultrasound-induced melatonin release of MKF is determined by UV–vis spectrophotometry. As shown in Fig. 4(a), the LC and EE values of MKF are 20.30 ± 0.32 % and 25.47 ± 0.51 %, respectively, and slightly lower than those of MK, maybe due to the depletion of melatonin during the wrapping of F127. As shown in Fig. 4(b), the absorbance and concentration are positively correlated. Fig. 4(c) shows the cumulative release of melatonin from MK and MKF at various ultrasound intensities (0, 1, 1.5, and 2 W/cm^2). The plots of MK with and without ultrasound are similar, proving the non-ultrasound responsiveness of melatonin. The CRR of the first 24 h accounts for more than 80 % of the entire 7 d cycle, demonstrating the characteristics of regular drug release. In contrast, the drug release efficiency of MKF improves with intensity. Particularly at 2 W/cm^2, the CRR reaches 72.45 ± 1.57 %, which is 28.35 % higher than that at 0 W/cm^2. Compared with MK, MKF prolongs the effective action period of the drug under the influence of ultrasound. This improves the problem associated with premature release and short total release time in conventional release systems, thus enabling the reduction of the drug dosage and prolonging the duty cycle.

The mechanism of ultrasound-induced drug delivery is related to the thermal and mechanical effects produced by ultrasound radiation. The thermal effect is caused by the conversion of acoustic energy into thermal energy, leading to a phase transition in the thermosensitive polymer to release the encapsulated drug [33]. However, according to Fig. 4(d), the CRRs of MKF at 37, 47, and 57 °C are almost the same, demonstrating that the release is temperature-independent. The mechanical effect denotes the transfer from acoustic energy into mechanical energy, primarily associated with cavitation [30]. The cavitation effect is evaluated by TA dosimetry, in which the ultrasonic cavitation converts hydroxyl groups in TA into free radicals with fluorescent property. The resulting product HTA exhibits a fluorescence peak around 425 nm. As illustrated in Fig. 4(e), it is indicated by the fluorescence intensity of HTA that the cavitation effect is directly

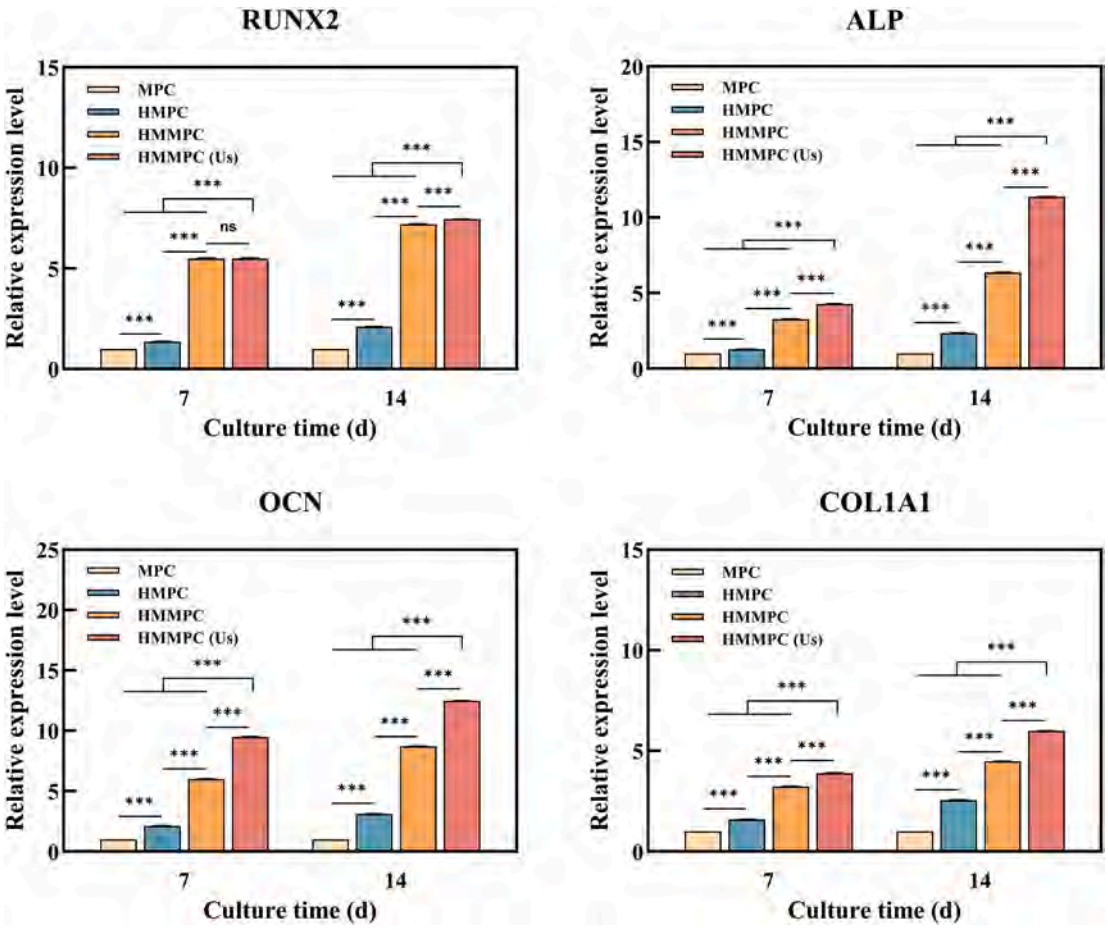

Fig. 12. Relative osteogenic mRNA expressions of Runx2, ALP, OCN, and COL1A1 (*p < 0.05, **p < 0.01, and ***p < 0.001).

proportional to sonication intensity. The GPC test further verifies how the cavitation alters F127. Fig. 4(f) shows that the number average molecular weight (Mn) of F127 increases from 2375 g/mol to 2731 g/mol, and the polymer dispersity (PD) decreases from 1.205 to 1.14 after 2 W/cm^2 sonication. Cavitation is a phenomenon where gaseous bubbles form, grow, and eventually collapse in the liquid during sonication. When bubbles burst, shear stress and shock waves are generated, resulting in reversible destabilization of the sonic-sensitive polymer [34–36]. The change of Mn implies an increase in the length of the polymer chain. As PD becomes closer to 1, the MW distribution becomes narrower, and the chain lengths are more even. Accordingly, F127 with a small MW may be polymerized due to ultrasound polymer synthesis. F127 (EO_a-PO_b-EO_c) is a triblock copolymer formed by the polymerization of propylene oxide (PO) and ethylene oxide (EO). It has been found that block copolymers can be formed through the combination of free radicals in 2–4 min by ultrasound [37]. Therefore, in our study, the cavitation effect cleaves F127 to produce active radicals EO_a·, PO_b· and EO_c· as initial materials, which may polymerize to form new copolymers EO_x-PO_y-EO_z with higher MW. The drug escapes from the F127 package in this process, as shown in Fig. 5. However, due to the non-block copolymer-forming side reactions, the specific mechanism of ultrasonic reaction remains incomplete and requires further investigation through more sophisticated characterizations in the future [38].

In contrast to endogenous responses, the exogenous ultrasound response is non-invasive, and the dosage can be controlled by regulating the power and duration in clinical practice [39]. Moreover, the advantages over other exogenous responses stem from the biological effect produced by cavitation [40,41]. The shear force and shock waves generated by the bubbles increase the porosity and permeability of the cell membrane, thereby enhancing intracellular drug uptake [42].

3.3. Characterization of cement

The phase composition is analyzed by XRD (Fig. 6a). The $MgKPO_4{\cdot}6H_2O$ peaks emerge at 20.974°, 21.579°, and 33.278°, and the MgO peaks are at 36.97°, 42.937°, 62.316°, and 78.63°, demonstrating that the crystal structure remains the same regardless of the addition of HA and MKF. As shown by the FTIR spectra in Fig. 6(b), in addition to O—H stretching (3500–2500 cm^{-1}) and H_2O bending (1630 cm^{-1}), the peaks at 1085 cm^{-1}, 808 cm^{-1}, and 549 cm^{-1} reveal PO_4^{3-} in $MgKPO_4{\cdot}6H_2O$. The HMPC and HMMPC samples also show C—H vibration (1410 cm^{-1}). The results are consistent with those obtained by EDS in Fig. 6(c) and Table. 2. As shown in Fig. 6(d), holes are obvious on the surface of MPC, while those on the other two samples become shallower. At the magnification of 2000× (Fig. 6e), the shape of $MgKPO_4{\cdot}6H_2O$ crystals is similar to that of struvite, which is prism growing along the b-axis based on the space group symmetry. After the addition of HA, the crystals shorten in the b-axis direction and elongate along the a-axis, accompanied by a general decrease in size [43]. The changes in the crystal morphology can be attributed to the adsorption of HA on the growing nuclei, pre-nucleation clusters and crystal surfaces [44]. The modified hydration products reduce the porosity and increase the compactness of the cement paste.

3.4. Handling properties and hydration reaction tests

As shown by the temperature variation curves in Fig. 7(a), the temperature of the cement rises rapidly, and the increasing rate declines until reaching the maximum at 7 (MPC) or 10 min (HMPC and HMMPC) and finally decreasing slowly to RT. Compared to the initial temperature, the maximum reaction temperature of MPC increases by 11.31 ±

0.46 °C (Fig. 7b), while that of HMPC is only 7.58 ± 1.02 °C, indicating that HA lowers the reaction temperature. According to Fig. 7(c), the setting time of MPC is 7.08 ± 0.31 min, and that of HMPC is 11.83 ± 0.47 min. Correspondingly, the injection rate and injection time of HMPC are higher than those of MPC (Table. 3). It is clear from the HMMPC data that the MKF nanocapsules have little effect on the temperature and time of the hydration reaction. Nevertheless, the addition of HA and MKF decreases the porosity and increases the density, consistent with the SEM images in Fig. 6(d). As the matrix becomes denser, the compressive strength of HMPC (27.12 ± 1.53 MPa) and HMMPC (30.19 ± 0.78 MPa) is higher, suggesting that the surgical applicability of MPC improves (Fig. 7d).

In order to improve the clinical viability of MPC, it is necessary to prolong the solidification time and lower the reaction temperature, so the hydration reaction process needs to be retarded. The hydration process of MPC is divided into three steps [45,46]:

I: MgO dissolves and releases Mg^{2+} and OH^-. Mg^{2+} undergoes a hydrolysis reaction with H_2O and creates a positively charged sol (Eqs. 6–7).

II: The sol reacts with K^+ and $H_2PO_4^-$ to form a loose phosphate gel (Eq. 8).

III: The gels saturate and precipitate to form well-connected ceramics with unreacted MgO as the nucleation points.

The dissolution and hydrolysis processes in step I are the controlling steps in forming MPC, and the acid-base reaction is exothermic. Their equations are simplified as below:

$$MgO + H_2O \rightarrow Mg^{2+}(aq) + 2OH^- \quad (6)$$

$$Mg^{2+}(aq) + H_2O \rightarrow Mg(OH)^+(aq) + H^+ \quad (7)$$

$$Mg(OH)^+ + K^+ + H_2PO_4^- + 5H_2O \rightarrow MgKPO_4 \cdot 6H_2O + H^+ \quad (8)$$

Combining the above formula and Fig. 7(e), the conductivities of the cement pastes rise rapidly, then increase slowly to the peak, and finally decline. Compared to the blank group, the initial rises in the conductivity of the HMPC and HMMPC groups are more gradual, which means the dissolution of MgO may be inhibited. The delay in the peak indicates that HA retards the saturation of the phosphate sol. The rate of conductivity decline slows down in the final stage, suggesting that HA probably influences the nucleation and crystallization processes of hydration products at step III. The overall changes in conductivity demonstrate that HA can inhibit the dissolution of reactants and the precipitation and growth of hydration products.

HA is a macromolecular polysaccharide, and according to previous research, the possible retardation mechanisms are based on the complexation theory and adsorption theory. The complexation theory refers to the formation of complexes between Mg^{2+} and carboxyl and hydroxyl groups in HA, which inhibit the hydrolysis reaction and delay the precipitation of hydration products [48]. If complexed Mg^{2+} with poor migration ability is generated, the conductivity of the system will decrease. From Fig. 7(f), excluding the inherent interference of HA, the conductivity of $MgCl_2$ solution decreases as HA concentration increases, indicating that HA induces complexation. Meanwhile, the complex effect becomes more pronounced with more hydroxyl and carboxyl groups. However, when the concentration reaches 5 mmol/L, the conductivity only decreases by 125 μS/cm. This means the complexation rate of HA for Mg^{2+} with the same concentration is only 9.55 %, making the complex effect relatively weak. The adsorption rates of HMPC and HMMPC obtained from the TOC test are 61.12 ± 1.60 % and 61.75 ± 2.73 %, respectively, implying strong adsorption effects of HA (Fig. 7g). It can be inferred that HA adsorbs onto the surface of the MgO particles to form a thin film and prevent them from reacting with water. They may also cover the surface of the hydration products to inhibit further growth, which is reflected in the slowing decrease in conductivity of the HMPC and HMMPC groups [49].

3.5. In vitro degradation

The cement samples were soaked in PBS for 21 days to determine the *in vitro* degradation behavior. As shown in Fig. 8(a), the compressive strength of the three cement samples keeps rising and reaches maximum values of 26.34 ± 2.95, 30.39 ± 4.12, and 32.44 ± 3.41 MPa on day 14 and then decreases until the 21st day. The trend in flexural strength is comparable, with the maximum value of 6.75 ± 0.16 MPa occurring on the 14th day in HMPC group (Fig. 8b). After three weeks of immersion, the compressive and flexural strengths of all three groups were generally higher than initial levels, demonstrating that the bone cements maintain stability during this period. As shown in Fig. 8(c), the WLR tends to increase overall. The MPC surface is corroded into fibers after 21 days, while the other two groups are in better condition (Fig. 8d). The compressive strength, flexural strength and WLR of HMPC and HMMPC are consistently superior to MPC throughout the immersion cycle, indicating the resistance to substrate corrosion. This is probably due to higher anchoring strength in the matrix and better cohesiveness with HA and MKF incorporation [50]. The change in compressive strength is perhaps influenced by two factors. The increase in the first 14 days may be dominated by the continuous transformation of hydration products and refinement of pores, while the decrease thereafter results from prevailing degradation [51,52].

3.6. Antibacterial properties

The antibacterial properties of the cement samples are assessed by the plate-counting method. As shown in Fig. 9(a), the largest number of colonies is found in the medium of the MPC group. The antibacterial rate of the HMPC group is higher than that of the MPC group (Fig. 9b), probably due to the ability of HA to retard bacterial adhesion and biofilm formation [53]. After the addition of MKF, the antibacterial ratio rises to 76.77 ± 1.06 %, suggesting that melatonin resists gram-negative bacteria by inhibiting bacterial citrate synthase [54]. Finally, 91.04 ± 1.44 % of the bactericidal effect is observed from the HMMPC (Us) group. The improvement may be attributed to melatonin release upon ultrasound treatment and reactive oxygen species (ROS) produced by sonodynamic therapy (SDT) [55]. The SDT efficacy occurs only when the acoustic sensitizers are combined with ultrasound stimulation to produce cytotoxic ROS that kill microorganisms.

3.7. In vitro biocompatibility

The *in vitro* biocompatibility is evaluated based on the proliferation, viability, and apoptosis of C3H10T1/2 cells. According to the fluorescence microscopy images after live/dead staining in Fig. 10(a), dead cells are absent from all the samples, indicating that MPC, HA, and drug-carrying nanocapsules are non-cytotoxic. As determined by flow cytometry, the cell apoptosis rate is the sum of late apoptotic cells (Q2 region in the scatter plot) and early apoptotic cells (Q3 region) (Fig. 10b). The apoptosis rates of the four groups are smaller than 4 %, with the lowest of 2.83 % observed from the HMMPC (Us) group (Fig. 10c). This demonstrates that the ultrasonically treated HMMPC inhibits apoptosis and is biocompatible *in vitro*. Furthermore, as shown in Fig. 10(d), the cell viability exhibits an overall upward trend during 5-day culturing. While the cell activity of the HMPC group and MPC group is similar, that of the HMMPC and HMMPC (Us) groups are enhanced on days 3 and 5, indicating promoted cell proliferation, with the most remarkable effect observed in HMMPC after sonication.

3.8. Osteogenic capacity

ALP staining, ARS staining, and osteogenic gene expression are performed to analyze the effects on osteogenic induction. As shown in Fig. 11(a), ALP and ARS staining is positive for the C3H10T1/2 cells treated with the four groups of cement extracts, indicating enhancement

in both early and late osteogenic differentiation. HA, MKF, and ultrasound treatment significantly ($p < 0.001$) improve the ALP activity (Fig. 11b), especially the HMMPC (Us) showing the highest ALP intensity. The ARS absorbance represents the degree of Ca^{2+} deposition and reflects the level of extracellular matrix (ECM) mineralization in the late differentiation stage. Similarly, the HMMPC (Us) group shows the highest level of mineralization, which is 2.88, 2.12, and 1.24 times higher than those of the other three groups, respectively (Fig. 11c). Quantification of ALP and ARS indicates that HMMPC (Us) has the optimal ability to improve early and late osteoclast differentiation. The expression levels of the osteogenesis-related transcription factor Runx2 and osteogenesis-specific matrix proteins ALP, OCN, and COL1A1 are measured. As shown in Fig. 12, the expression levels of these genes in the MPC group are comparable after the 7th and 14th days, implying little facilitating effects. The expression levels are higher than that of the MPC group. In particular, the HMMPC (Us) group shows the most significant up-regulation ($p < 0.001$), suggesting the optimal promotion of osteogenic differentiation by HA and MKF after the ultrasound treatment.

4. Conclusions

The magnesium phosphate bone cement HMMPC doped with HA and ultrasound-responsive melatonin-loaded nanosilica MKF is prepared. The complexation and adsorption of HA retards the hydration of HMMPC, giving rise to superior physicochemical properties compared to conventional MPC. HMMPC has a reaction temperature of 31.41 ± 0.79 °C, a setting time of 11.9 ± 0.78 min, and an injectability of 90.36 ± 4.01 %, boding well for surgical applications. The cavitation mechanism of ultrasound-triggered drug release is investigated, and drug release can be controlled by modulating the intensity and duration of ultrasound to improve the effective duration and utilization. *In vitro* assessment corroborates the excellent antibacterial properties, cytocompatibility, as well as osteogenic capacity. The favorable compressive strength, degradation resistance, antimicrobial properties, biocompatibility, and osteogenesis render it a viable bone substitute. Nevertheless, several limitations are presented by this study. Firstly, the potential damage that ultrasound cavitation could inflict on surrounding cells and tissues requires systematic evaluation. What's more, the long-term reliability and stability of cements remain to be tested through fatigue performance and dynamic load response. Most importantly, the clinical efficacy of HMMPC is still unknown due to the lack of *in vivo* experiments. In summary, while this research reveals an effective strategy for developing multifunctional cement for orthopedics, the ultimate clinical translation depends on further investigation.

CRediT authorship contribution statement

Junyan Yao: Investigation, Methodology, Software, Writing – original draft. **Bin Wang:** Methodology, Writing – original draft. **Yanbin Zhao:** Writing – review & editing. **Yingxi Xu:** Writing – review & editing. **Cheng Wang:** Supervision. **Jing Bai:** Funding acquisition. **Feng Xue:** Project administration. **Paul K. Chu:** Funding acquisition, Writing – review & editing. **Chenglin Chu:** Funding acquisition, Writing – review & editing.

Declaration of competing interest

The authors declare that they have no known competing financial interests or personal relationships that could have appeared to influence the work reported in this paper.

Acknowledgments

This work was supported by the National Natural Science Foundation of China (Grant number 52171236), State Key Program of the National Natural Science Foundation of China (Grant number 52231005), Open Research Fund of Jiangsu Key Laboratory for Advanced Metallic Materials, Southeast University (Grant number AMM2024A01), Suzhou Science and Technology Project (Grant numbers SJC2023005, SZS2023023), City University of Hong Kong Donation Research Grants (DON-RMG 9229021 and 9220061), and Guangdong - Hong Kong Technology Cooperation Funding Scheme (TCFS GHP/212/22GD and CityU 9440399).

Data availability

Data will be made available on request.

References

[1] S. De Lacerda Schickert, J.C. Pinto, J. Jansen, S.C.G. Leeuwenburgh, J.J.J.P. Van Den Beucken, Tough and injectable fiber reinforced calcium phosphate cement as an alternative to polymethylmethacrylate cement for vertebral augmentation: a biomechanical study, Biomater. Sci. 8 (15) (2020) 4239–4250.
[2] Y. Zhao, P. He, J. Yao, M. Li, B. Wang, L. Han, Z. Huang, C. Guo, J. Bai, F. Xue, Y. Cong, W. Cai, P.K. Chu, C. Chu, pH/NIR-responsive and self-healing coatings with bacteria killing, osteogenesis, and angiogenesis performances on magnesium alloy, Biomaterials 301 (2023) 122237.
[3] E.D. Arrington, W.J. Smith, H.G. Chambers, A.L. Bucknell, N.A. Davino, Complications of Iliac Crest Bone Graft Harvesting, Clin. Orthop. Relat. R. 329 (1996) 300–309.
[4] X. Gu, Y. Li, C. Qi, K. Cai, Biodegradable magnesium phosphates in biomedical applications, J. Mater. Chem. B 10 (13) (2022) 2097–2112.
[5] Y. Zhao, Y. Li, B. Wang, J. Yao, Y. Fan, P. He, J. Bai, C. Wang, F. Xue, C. Chu, An injectable magnesium-based cement stimulated with NIR for drug-controlled release and osteogenic potential, Adv. Healthc. Mater. 13 (19) (2024) 2400207.
[6] H. Zhou, A.K. Agarwal, V.K. Goel, S.B. Bhaduri, Microwave assisted preparation of magnesium phosphate cement (MPC) for orthopedic applications: A novel solution to the exothermicity problem, Mater. Sci. Eng. C 33 (7) (2013) 4288–4294.
[7] J. Qin, J. Qian, X. Dai, C. You, H. Ma, Z. Li, Effect of water content on microstructure and properties of magnesium potassium phosphate cement pastes with different magnesia-to-phosphate ratios, J. Am. Ceram. Soc. 104 (6) (2021) 2799–2819.
[8] A. Viani, P. Mácová, Polyamorphism and frustrated crystallization in the acid–base reaction of magnesium potassium phosphate cements, CrystEngComm 20 (32) (2018) 4600–4613.
[9] L. Yu, T. Gao, W. Li, J. Yang, Y. Liu, Y. Zhao, P. He, X. Li, W. Guo, Z. Fan, H. Dai, Carboxymethyl chitosan-alginate enhances bone repair effects of magnesium phosphate bone cement by activating the FAK-Wnt pathway, Bioact. Mater. 20 (2023) 598–609.
[10] T. Ma, J. Liao, Y. Zhang, J. Feng, Y. Yang, H. Li, W. Guo, J. Chen, Study on modification of hydroxyapatite/magnesium phosphate bone cement by N-acetyl-l-cysteine, Ceram. Int. 49 (11) (2023) 16545–16553.
[11] J. Chen, L. Yu, T. Gao, X. Dong, S. Li, Y. Liu, J. Yang, K. Xia, Y. Yu, Y. Li, S. Wang, Z. Fan, H. Deng, W. Guo, Nanofiber-induced hierarchically-porous magnesium phosphate bone cements accelerate bone regeneration by inhibiting Notch signaling, Bioact. Mater. 37 (2024) 459–476.
[12] J. Liu, J. Zhu, T. Goto, S. Yang, H. Kang, X. Wang, H. Dai, Modulation of bone homeostasis by dual drug-loaded premixed magnesium tri-magnesium phosphate bone cement for the treatment of osteoporotic vertebral compression fractures, Bioact. Mater. 54 (2025) 631–647.
[13] P. He, Y. Zhao, B. Wang, Y. Wang, Y. Li, M. Li, C. Chu, B. Xu, Y. Cong, An injectable and absorbable magnesium phosphate bone cement designed for osteoporotic fractures, Mater. Today Chem. 38 (2024).
[14] F. Xing, C. Zhou, D. Hui, C. Du, L. Wu, L. Wang, W. Wang, X. Pu, L. Gu, L. Liu, Z. Xiang, X. Zhang, Hyaluronic acid as a bioactive component for bone tissue regeneration: Fabrication, modification, properties, and biological functions, Nanotechnol. Rev. 9 (1) (2020) 1059–1079.
[15] Y. Zhao, P. He, J. Yao, M. Li, J. Bai, F. Xue, C. Chu, Y. Cong, P.K. Chu, Self-assembled multilayered coatings with multiple cyclic self-healing capability, bacteria killing, osteogenesis, and angiogenesis properties on magnesium alloys, Adv. Healthc. Mater. 13 (9) (2024) 2302519.
[16] M.C.G. Juenger, H.M. Jennings, New insights into the effects of sugar on the hydration and microstructure of cement pastes, Cem. Concr. Res. 32 (3) (2002) 393–399.
[17] Z. Xiaowei, L. Chunxia, S. Junyi, Influence of tartaric acid on early hydration and mortar performance of Portland cement-calcium aluminate cement-anhydrite binder, Constr. Build. Mater. 112 (2016) 877–884.
[18] H. Zhu, N. Mitsuhashi, A. Klein, L.W. Barsky, K. Weinberg, M.L. Barr, A. Demetriou, G.D. Wu, The Role of the Hyaluronan Receptor CD44 in Mesenchymal Stem Cell Migration in the Extracellular Matrix, Stem Cells 24 (4) (2006) 928–935.
[19] U. Hempel, C. Preissler, S. Vogel, S. Möller, V. Hintze, J. Becher, M. Schnabelrauch, M. Rauner, L.C. Hofbauer, P. Dieter, Artificial Extracellular Matrices with Oversulfated Glycosaminoglycan Derivatives Promote the Differentiation of Osteoblast-Precursor Cells and Premature Osteoblasts, Biomed. Res. Int. 2014 (2014) 1–10.

[20] J.R. Schmidt, S. Vogel, S. Moeller, S. Kalkhof, K. Schubert, M. Von Bergen, U. Hempel, Sulfated hyaluronic acid and dexamethasone possess a synergistic potential in the differentiation of osteoblasts from human bone marrow stromal cells, J. Cell. Biochem. 120 (5) (2019) 8706–8722.
[21] P. Zhai, X. Peng, B. Li, Y. Liu, H. Sun, X. Li, The application of hyaluronic acid in bone regeneration, Int. J. Biol. Macromol. 151 (2020) 1224–1239.
[22] T. Li, S. Jiang, C. Lu, W. Yang, Z. Yang, W. Hu, Z. Xin, Y. Yang, Melatonin: Another avenue for treating osteoporosis? J. Pineal Res. 66 (2) (2019) e12548.
[23] V. Polshettiwar, D. Cha, X. Zhang, J.M. Basset, High-Surface-Area Silica Nanospheres (KCC-1) with a Fibrous Morphology, Angew. Chem. Int. Edit. 49 (50) (2010) 9652–9656.
[24] S.M. Mirvakili, R. Langer, Wireless on-demand drug delivery, Nat. Electron. 4 (7) (2021) 464–477.
[25] Z. Wang, Q. He, W. Zhao, J. Luo, W. Gao, Tumor-homing, pH- and ultrasound-responsive polypeptide-doxorubicin nanoconjugates overcome doxorubicin resistance in cancer therapy, J. Control. Release 264 (2017) 66–75.
[26] S. Chu, X. Shi, Y. Tian, F. Gao, pH-Responsive Polymer Nanomaterials for Tumor Therapy, Front. Oncol. 12 (2022) 855019.
[27] H. Chen, Y. Jin, J. Wang, Y. Wang, W. Jiang, H. Dai, S. Pang, L. Lei, J. Ji, B. Wang, Design of smart targeted and responsive drug delivery systems with enhanced antibacterial properties, Nanoscale 10 (45) (2018) 20946–20962.
[28] X. Wang, Z. Xuan, X. Zhu, H. Sun, J. Li, Z. Xie, Near-infrared photoresponsive drug delivery nanosystems for cancer photo-chemotherapy, J. Nanobiotechnol. 18 (1) (2020) 108.
[29] Y. Zhao, P. He, B. Wang, J. Bai, F. Xue, C. Chu, Incorporating pH/NIR responsive nanocontainers into a smart self-healing coating for a magnesium alloy with controlled drug release, bacteria killing and osteogenesis properties, Acta Biomater. 174 (2024) 463–481.
[30] T.J. Yeingst, J.H. Arrizabalaga, D.J. Hayes, Ultrasound-Induced Drug Release from Stimuli-Responsive Hydrogels, Gels 8 (9) (2022) 554.
[31] B. Lyons, J.P.R. Balkaran, D. Dunn-Lawless, V. Lucian, S.B. Keller, C.S. O'Reilly, L. Hu, J. Rubasingham, M. Nair, R. Carlisle, E. Stride, M. Gray, C. Coussios, Sonosensitive cavitation nuclei—a customisable platform technology for enhanced therapeutic delivery, Molecules 28 (23) (2023) 7733.
[32] J. Xu, J. Zhang, H. Peng, X. Xu, W. Liu, Z. Wang, N. Zhang, X. Wang, Ag supported on meso-structured SiO 2 with different morphologies for CO oxidation: On the inherent factors influencing the activity of Ag catalysts, Microporous Mesoporous Mater. 242 (2017) 90–98.
[33] P. Wei, E.J. Cornel, J. Du, Ultrasound-responsive polymer-based drug delivery systems, Drug Deliv. Transl. Res. 11 (4) (2021) 1323–1339.
[34] Q.-L. Zhou, Z.-Y. Chen, Y.-X. Wang, F. Yang, Y. Lin, Y.-Y. Liao, Ultrasound-Mediated Local Drug and Gene Delivery Using Nanocarriers, Biomed. Res. Int. 2014 (2014) 1–13.
[35] K. Kooiman, S. Roovers, S.A.G. Langeveld, R.T. Kleven, H. Dewitte, M.A. O'Reilly, J.M. Escoffre, A. Bouakaz, M.D. Verweij, K. Hynynen, I. Lentacker, E. Stride, C. K. Holland, Ultrasound-Responsive Cavitation Nuclei for Therapy and Drug Delivery, Ultrasound Med. Biol. 46 (6) (2020) 1296–1325.
[36] B. Yang, J. Du, On the origin and regulation of ultrasound responsiveness of block copolymer nanoparticles, Sci. China Chem. 63 (2) (2020) 272–281.
[37] A.H. Lebovitz, M.K. Gray, A.C. Chen, J.M. Torkelson, Interpolymer radical coupling reactions during sonication of polymer solutions, Polymer 44 (10) (2003) 2823–2828.
[38] T.G. McKenzie, F. Karimi, M. Ashokkumar, G.G. Qiao, Ultrasound and Sonochemistry for Radical Polymerization: Sound Synthesis, Chem-Eur. J. 25 (21) (2019) 5372–5388.
[39] L.J. Delaney, S. Isguven, J.R. Eisenbrey, N.J. Hickok, F. Forsberg, Making waves: how ultrasound-targeted drug delivery is changing pharmaceutical approaches, Mater. Adv. 3 (7) (2022) 3023–3040.
[40] C.-H. Li, Y.-C. Chang, M. Hsiao, M.-H. Chan, Ultrasound and Nanomedicine for Cancer-Targeted Drug Delivery: Screening, Cellular Mechanisms and Therapeutic Opportunities, Pharmaceutics 14 (6) (2022) 1282.
[41] J. Tu, A.C.H. Yu, Ultrasound-Mediated Drug Delivery: Sonoporation Mechanisms, Biophysics, and Critical Factors, Bme. Front. 2022 (2022) 9807347.
[42] K. Entzian, A. Aigner, Drug Delivery by Ultrasound-Responsive Nanocarriers for Cancer Treatment, Pharmaceutics 13 (8) (2021) 1135.
[43] A. Viani, P. Mácová, R. Ševčík, L. Zárybnická, Mechanism of magnesium phosphate cement retardation by citric acid, Ceram. Int. 49 (7) (2023) 11112–11122.
[44] A. Viani, L. Zárybnická, R. Ševčík, P. Mácová, J. Machotová, K. Veltruská, Struvite-K crystal growth inhibition by citric acid: Formation of complexes in solution and surface adsorption effects, J. Cryst. Growth 598 (2022) 126858.
[45] A.S. Wagh, S.Y. Jeong, Chemically Bonded Phosphate Ceramics: I, A Dissolution Model of Formation, J. Am. Ceram. Soc. 86 (11) (2003) 1838–1844.
[46] M. Le Rouzic, T. Chaussadent, G. Platret, L. Stefan, Mechanisms of k-struvite formation in magnesium phosphate cements, Cem. Concr. Res. 91 (2017) 117–122.
[48] M.A. Haque, B. Chen, Research progresses on magnesium phosphate cement: A review, Constr. Build. Mater. 211 (2019) 885–898.
[49] X. Yu, C. Yu, Q. Ran, J. Liu, Retarding Mechanism of Hydroxy Carboxylic Acid Retarder on Cement Hydration, J. Chin. Ceram. Soc. 46 (2) (2018) 181–186.
[50] Y. Liu, Y. Wu, H. Lin, Y. Xiao, X. Zhu, K. Zhang, Y. Fan, X. Zhang, Study on an injectable biomedical paste using cross-linked sodium hyaluronate as a carrier of hydroxyapatite particles, Carbohydr. Polym. 195 (2018) 378–386.
[51] X. Cui, C. Huang, Z. Chen, M. Zhang, C. Liu, K. Su, J. Wang, L. Li, R. Wang, B. Li, D. Chen, C. Ruan, D. Wang, W.W. Lu, H. Pan, Hyaluronic acid facilitates bone repair effects of calcium phosphate cement by accelerating osteogenic expression, Bioact. Mater. 6 (11) (2021) 3801–3811.
[52] G. Zhang, Q. Wang, Y. Li, M. Zhang, Microstructure and micromechanical properties of magnesium phosphate cement, Cem. Concr. Res. 172 (2023) 107227.
[53] F. Zamboni, C.K. Wong, M.N. Collins, Hyaluronic acid association with bacterial, fungal and viral infections: Can hyaluronic acid be used as an antimicrobial polymer for biomedical and pharmaceutical applications? Bioact. Mater. 19 (2023) 458–473.
[54] F. He, X. Wu, Q. Zhang, Y. Li, Y. Ye, P. Li, S. Chen, Y. Peng, R. Hardeland, Y. Xia, Bacteriostatic Potential of Melatonin: Therapeutic Standing and Mechanistic Insights, Front. Immunol. 12 (2021) 683879.
[55] H. Liu, J. Li, X. Liu, Z. Li, Y. Zhang, Y. Liang, Y. Zheng, S. Zhu, Z. Cui, S. Wu, Photo-Sono Interfacial Engineering Exciting the Intrinsic Property of Herbal Nanomedicine for Rapid Broad-Spectrum Bacteria Killing, ACS Nano 15 (11) (2021) 18505–18519.